

# Multi-flavor quantum criticality

A. Khansili,<sup>1</sup> A. Bangura,<sup>2</sup> R.D. McDonald,<sup>3</sup> B.J. Ramshaw,<sup>4</sup> A. Rydh,<sup>1</sup> and

A. Shekhter<sup>3,\*</sup>

<sup>1</sup>*Department of Physics, Stockholm University, SE-106 91 Stockholm, Sweden*

<sup>2</sup>*National High Magnetic Field Laboratory, Tallahassee Florida 32310, USA*

<sup>3</sup>*Los Alamos National Laboratory, Los Alamos New Mexico 87545, USA*

<sup>4</sup>*Laboratory of Atomic and Solid State Physics, Cornell University, Ithaca New York 14853 USA*

(Dated: November 21, 2023)

In a quantum critical metal, the electronic density of states, or quasiparticle mass on the Fermi surface, is strongly enhanced through electronic correlations. The density of states in the quantum critical unconventional superconductor CeCoIn<sub>5</sub>, can be readily accessed in the normal state because all energy scales are small. However, the experimental challenges associated with large nuclear specific heat and long nuclear spin-lattice relaxation times have impeded unveiling a more detailed physical picture. Here we report an extensive thermal impedance spectroscopy study of CeCoIn<sub>5</sub> that assesses the density of states in two independent ways, via the nuclear spin-lattice relaxation rate and via the specific heat. We establish that the temperature- and magnetic field dependence of the nuclear spin-lattice relaxation rate is determined entirely by the energy-scale competition near the quantum critical point. In particular, mass enhancement is cut off at finite magnetic fields. However, the specific heat measurements reveal excess entropy in addition to that associated with the density of states on the Fermi surface. This excess entropy is direct thermodynamic evidence for a “second flavor” of fluctuating boson in CeCoIn<sub>5</sub>. The electronic nature of this excess entropy is evidenced by its suppression in the superconducting state. We suggest such a multi-flavor character for a broader class of quantum critical metals.

---

\*Email: arkadyshekhter@gmail.com

## 1. INTRODUCTION

The heavy-fermion metal  $\text{CeCoIn}_5$  is a commensurate end member of a chemical doping series of antiferromagnetic (AFM) compounds (1–6). In this series,  $\text{CeCoIn}_5$  borders the zero-temperature collapse of the AFM transition. A strong increase in the electronic density of states at low temperatures, evidenced by specific heat (7–9) and nuclear spin-lattice relaxation rate measurements (10–16), has generated broad interest in the quantum criticality in  $\text{CeCoIn}_5$  (17–21). Electric transport studies of  $\text{CeCoIn}_5$  show  $T$ -linear resistivity and  $1/T^2$  behavior of the Hall angle over a broad temperature range (22), similar to quantum criticality in the cuprates (23; 24).

Specific heat and nuclear spin-lattice relaxation rate studies of  $\text{CeCoIn}_5$  in magnetic field have allowed a more detailed picture of its quantum criticality (8–15; 25–28). In particular, the strong increase of the electronic density of states is suppressed in magnetic fields (7; 14; 15), which is a sign of an energy-scale competition near the quantum critical point, characteristic of a broader class of quantum critical systems (24; 29).

To gain further insight into the microscopic working of quantum criticality in  $\text{CeCoIn}_5$ , it is necessary to contrast the density of states as determined by multiple independent techniques. The newly developed thermal impedance spectroscopy (TISP) technique (30) offers a unique avenue to explore such energy-scale competition in  $\text{CeCoIn}_5$  through two simultaneous but independent experimental pathways of accessing the electronic density of states: as inferred from specific heat measurements and from nuclear spin-lattice relaxation. While both probe the density of states on the Fermi surface, specific heat also accesses the entropy of all low-energy excitations, including those outside the Fermi surface.

## 2. RESULTS

Figure 1 shows the nuclear spin-lattice relaxation rate divided by temperature  $1/T_1T$  (Figure 1e) and the electronic specific heat divided by temperature  $C/T$  (Figure 1f) at 12 T above the superconducting transition in  $\text{CeCoIn}_5$  (dashed line in Figure 1c) for different magnetic field orientations. In conventional metals,  $1/T_1T$  is proportional to the square of the electronic density of states on the Fermi surface (31; 32) as well as Landau parameters associated with the electron-electron interactions (33–36). In  $\text{CeCoIn}_5$ , the spin-lattice relaxation rate increases strongly with decreasing temperature in the normal state, approxi-

mately as a power law  $T_1 \propto 1/T^{1/4}$  (grey line in Figure 1e), consistent with nuclear magnetic resonance (NMR) and nuclear quadrupole resonance (NQR) measurements (10) as well as theoretical expectations (34; 35). As we decrease temperature at fixed applied magnetic field  $B$ ,  $1/T_1T$  plateaus to a temperature-independent value below an angular- (and field-) dependent crossover temperature  $T_\alpha(B, \theta)$  (Figure 1e). In conventional metals, the electronic part of  $C/T$  is proportional to the density of states on the Fermi surface, which is weakly dependent on temperature and magnetic field (37; 38). In contrast, in CeCoIn<sub>5</sub>,  $C/T$  (Figure 1f) increases by a factor of 25 from a heavy-fermion value of 200 mJ/mol K<sup>2</sup> at 10 K (well below the coherence temperature (39; 40)) to about 5000 mJ/mol K<sup>2</sup> at 0.1 K.  $C/T$  also exhibits a crossover at  $T_\alpha(B, \theta)$ .

Unlike  $1/T_1T$ ,  $C/T$  continues to increase, albeit at a different rate, below the crossover temperature  $T_\alpha(B, \theta)$  down to the lowest measured temperature. We emphasize that in our measurements, such increase in the electronic specific heat below  $T_\alpha(B, \theta)$  cannot be attributed to the Schottky anomaly of the nuclear specific heat, since thermal impedance spectroscopy determines the electronic and the nuclear parts of the specific heat through their distinct spectral (frequency dependence) signatures. Figure 1g shows the nuclear specific heat, determined by thermal impedance spectroscopy *independently* from electronic specific heat (30). In contrast, conventional specific heat measurements (7; 8) require proper subtraction of the nuclear specific heat.

Figure 1d shows the angular dependence of  $T_\alpha(B, \theta)$  as inferred from the nuclear spin-lattice relaxation in Figure 1e. The effect of magnetic field strength on  $T_\alpha(B, \theta)$  is shown in Figure 2, where the magnetic field strength is varied, for three field directions. The saturation of  $1/T_1T$  below  $T_\alpha(B, \theta)$  in Figure 2d,e,f defines the magnetic field dependence of  $T_\alpha(B, \theta)$ , as indicated by vertical arrows.

The temperature scale  $T_\alpha(B, \theta)$  corresponds, equivalently, to a crossover magnetic field  $B_\alpha(T, \theta)$ . The superconducting transition at  $B_{c2}(T)$  determined from specific heat in Figure 2abc, together with  $B_\alpha(T, \theta)$  are shown in Figure 3. The crossover field  $B_\alpha(B, \theta)$  is linearly proportional to temperature,  $B_\alpha(T, \theta) \propto T$ , which defines an angular-dependent  $q$ -factor function  $q(\theta) = T_\alpha(B, \theta)/B = T/B_\alpha(T, \theta)$ . The angular dependence of  $q(\theta)$  follows the lowest (uniaxial) angular harmonics in the tetragonal CeCoIn<sub>5</sub> structure,  $q^2(\theta) = q_c^2 \cos^2 \theta + q_{ab}^2 \sin^2 \theta$ . The in-plane  $q_{ab} = 30 \pm 5$  mK/T and out-of plane  $q_c = 70 \pm 5$  mK/T (see Figure S6) are both anomalously small, which indicates a small energy scale associated

with the magnetic field in the quantum critical CeCoIn<sub>5</sub>, or equivalently, large crossover fields: it takes 30 T magnetic field applied along the *ab*-plane for the crossover temperature to reach 1 K.

### 3. DISCUSSION

The observed nuclear spin lattice relaxation rate  $1/T_1T$  reveals that all of the dependence of the electronic density of states (mass on the Fermi surface) on temperature and magnetic field is determined solely through their effect on a cutoff scale  $\Lambda(B, T)$ . At zero field, this cutoff is given by temperature,  $\Lambda(T, B = 0) = k_B T$ . At finite magnetic fields,  $1/T_1T$  is given entirely by the competition of the temperature and magnetic field to set the cutoff scale,  $\Lambda(T, B, \theta) \propto k_B \max\{T, T_\alpha(B, \theta)\}$ . Thus,  $k_B T_\alpha(B, \theta)$  (or  $k_B q(\theta) B_\alpha(T, \theta)$ ) is the competing energy scale associated with an applied magnetic field. The nuclear spin-lattice relaxation rate saturates below  $T_\alpha(B, \theta)$  in Figure 2d,e,f because the cutoff  $\Lambda$  there is set by magnetic field, and therefore depends weakly on temperature.

The energy-scale competition is directly observed at very high magnetic fields where magnetic field sets the dominant energy scale. Figure 4 shows the monotonic decrease of both  $1/T_1T$  and  $C/T$  with field in the normal state. In this regime, the decrease of both  $1/T_1T$  and  $C/T$  can be attributed to the decrease of electronic density of states on the Fermi surface. From the entropy point of view, the divergence of the electronic density of state (quasiparticle mass) at low temperatures implies a pileup of electronic states at lower and lower energies, i.e., the continual transfer of entropy from far away from the Fermi surface (but still below the coherence scale in CeCoIn<sub>5</sub>) to the Fermi level. Magnetic field cuts off this entropy pileup at energies below the magnetic field energy scale  $k_B T_\alpha$ . This magnetic-field driven suppression of the low-energy entropy pileup persists to the highest measured fields (Figure 4).

In the superconducting state, the nuclear spin-lattice relaxation rate approaches zero at low magnetic fields (41), dropping by a factor of 10 from 5 T – just above the upper critical field  $B_{c2}$  along the *c*-axis – to 2 T (Figure 2d). [As one moves to zero field, the  $1/T_1T$  is expected to become zero at low temperatures, as is observed in zero-field NQR measurements (42).] Similarly,  $C/T$  is strongly suppressed at low temperatures as we turn off magnetic field, with about 5% residual specific heat at zero field (Figure 2a). This shows that over

the entire temperature range, about 95% of the  $C/T$  is generated at the Fermi surface (see Figure S6).

The temperature-dependent mass renormalization is commonly attributed to the self-energy effects of interactions with a “boson” that has quantum critical dynamics (18; 20; 24; 29; 43). The magnetic field dependence of the electronic density of state on the Fermi surface is a result of the interaction of this boson with magnetic field. Figure 3 shows that the B-linear dependence of  $T_\alpha$  is not affected by superconductivity when crossing the superconducting phase boundary  $B_{c2}$ . Thus, this boson exhibits “no-feedback” behavior (44; 45), i.e., its dynamics is not affected by superconductivity. This is in a direct analogy with the discussion of A-phase superconductivity (44) in  $^3\text{He}$ . This no-feedback behavior implies that the boson originates from outside the Fermi surface, e.g., from localized  $f$ -electron states. Together with the itinerant aspect of the  $f$ -electrons in  $\text{CeCoIn}_5$ , being a heavy fermion metal, it follows that  $f$ -electrons in  $\text{CeCoIn}_5$  have both itinerant and localized character. The strong magnetic field required to suppress the mass renormalization (30 T at 1 K) indicates that the fluctuating local states are not directly associated with isolated  $f$ -orbital states, but comprise collective dynamics of many such states.

At low magnetic fields in the superconducting state,  $1/T_1T$  and  $C/T$  increase monotonically as a result of the increasing number of vortices in the superconducting state (Figure 2). The effective density of states at the chemical potential is finite in magnetic field because the moving condensate boosts the spectrum of the Bogoliubov-deGennes quasiparticles (46) in the reference frame of the lattice (41; 47; 48). Such superconducting effects at low magnetic fields are superseded by the cutoff behavior of the effective mass at high magnetic fields, creating a maximum at intermediate fields as observed in Figure 4. This non-monotonic behavior of the density of states, most apparent along the  $c$ -axis, has been discussed (8; 14; 15; 25; 26) in terms of field-induced quantum criticality, i.e., a *thermodynamic* tuning of the quantum critical behavior by magnetic field (21). In contrast, our discussion of the observed behavior requires only *dynamic* cutoff effects of the quantum criticality.

It is interesting, that the field dependence in Figure 4a is sharp at the lowest temperatures, whereas the field scan at 0.5 K exhibits a broad plateau extending from 5 T to 10 T. This can be understood by comparing the behavior of crossover field  $B_\alpha(T)$  and critical field  $B_{c2}(T)$  in Figure 3. At 0.12 K, the crossover field is close to  $B_{c2}$ . On the other hand, at 0.5 K, the

crossover field is a factor of two larger than  $B_{c2}$ . This implies that at 0.12 K, the decrease in  $C/T$ , driven by the magnetic field dependence of the cutoff, sets in right around  $B_{c2}$ , whereas at 0.5 K, this decrease only sets in at around 10 T. The non-monotonic magnetic field dependence of the nuclear spin-lattice relaxation rate in Figure 4 can be understood along the same lines of argument.

The entropy pileup in the normal state density of states can be directly observed *through* the entropy of the superconducting state. In superconductors, the entropy at  $T_c$  (integrated area under electronic  $C(T)/T$  up to  $T_c$ ) must be the same for both superconducting and underlying “hypothetical” normal states (41; 49). In CeCoIn<sub>5</sub>, the superconducting state has excess entropy in zero field, as indicated in part by the anomalously large superconducting jump  $\Delta C/C \approx 4$ . Thus, the underlying (zero field) normal state must have the same excess entropy at  $T_c$ . While the underlying zero field density of states is not directly accessible, we expect its entropy at  $T_c$  to be close to that of the normal state at 12 T along the *ab*-plane, where the magnetic field cutoff is still small. Indeed, the entropy in zero-field (integrating zero-field curve in Figure 2a) is close to that in 12 T along the *ab*-plane in the normal state (see Figure E4). The excess entropy of the superconducting state is a result of an uninterrupted entropy pileup in the underlying normal state driven by quantum criticality. This gives direct thermodynamic evidence that the quantum critical fluctuations and the superconducting behavior are two independent – no-feedback – effects that together determine the observed  $C/T$  behavior.

It is peculiar, that the entropy pileup is not completely frozen below the magnetic field cutoff, as indicated by the continual increase of  $C/T$  in the normal state below the crossover temperature  $T_\alpha(B, \theta)$  (Figure 1f and Figure 2a,c,e). This suggests physics beyond the mass renormalization on the Fermi surface. Such temperature-dependent  $C/T$  below  $T_\alpha(B, \theta)$  is evidence of a second “flavor” of electronic boson. Because the entropy pileup continues below  $T_\alpha(B, \theta)$  at all fields in the normal state in Figure 2, the magnetic field energy scale for the dynamics of the second boson is much smaller compared to the boson responsible for mass renormalization. Consistent with this, the second boson flavor does not directly – or indirectly, via mass renormalization – contribute to the nuclear spin-lattice relaxation rate. It is thus non-magnetic, i.e., it is not associated with electron spin flips.

In the normal state, the critical fluctuations of this second boson flavor account for an increase in  $C/T$  of more than 500 mJ/molK<sup>2</sup> at 0.12 K below the crossover temperature for

fields along the  $c$ -axis (Figure 1). However, the residual  $C/T$  at 0.12 K in the superconducting state at zero field is much smaller (Figure 2). Thus, the entropy associated with the second boson is mostly suppressed (gapped out) by the superconductivity. Therefore, the second boson exhibits feedback behavior, i.e., its fluctuations are suppressed below  $T_c$  in zero field. Such feedback behavior of the second boson implies that it lives on the Fermi surface, somewhat similar to spin fluctuations in  $^3\text{He}$  (44; 50), or mixed valence fluctuations in the related compound  $\text{PuCoGa}_5$  (43).

We anticipate that a broad range of quantum critical metals has a multi-flavor character similar to that established here for  $\text{CeCoIn}_5$ .

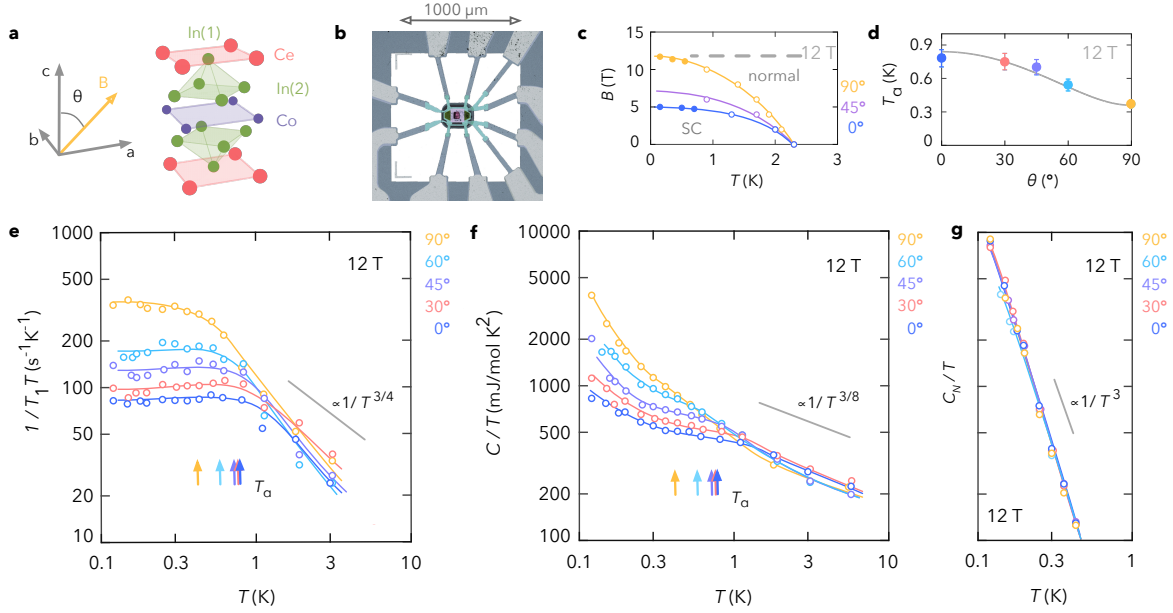


**FIG. 1 Angular dependence of  $1/T_1T$  and  $C/T$  at 12 T.** **a.** Angular convention for magnetic field orientation adopted in this study and the tetragonal unit cell of  $\text{CeCoIn}_5$ . **b.** Color-enhanced optical image of the calorimeter platform with mounted sample. **c.** Superconducting phase diagram determined from specific heat measurements. Open markers indicate  $B_{c2}$  determined from  $C/T$  in Figure 2, and filled markers from AC-calorimetry (see Figure E1). The horizontal gray dashed line shows the measurement “trajectory” for data in panels e,f,g. **d.** Angular dependence of the crossover temperature  $T_\alpha(B, \theta)$  of panels e,f. Solid curve represent anisotropic uniaxial behavior  $q^2(\theta) = q_c^2 \cos^2 \theta + q_{ab}^2 \sin^2 \theta$  with  $q_{ab} = 30 \pm 5$  mK/T and  $q_c = 70 \pm 5$  mK/T. **e.** Temperature dependence of  $1/T_1T$  for different field orientations  $\theta$ . Each curve shows a saturation below the crossover temperature  $T_\alpha(B = 12T, \theta)$ , indicated by the vertical arrows (evaluation described in Figure S3). The gray line indicates the expected normal-state temperature of  $1/T_1T$  near the AFM quantum critical point (35). **f.** Corresponding temperature dependence of the sample specific heat, excluding its nuclear specific heat. The vertical arrows represent  $T_\alpha(B = 12T, \theta)$  determined from panel e. Solid line represents the negative 3/8 power. **g.** Nuclear specific heat  $C_N/T$  of the sample is determined independently by its spectral signature. Solid line represents  $C_N \propto 1/T^2$ . For a detailed comparison, see Section 5.O. Solid curves are guides for the eye.



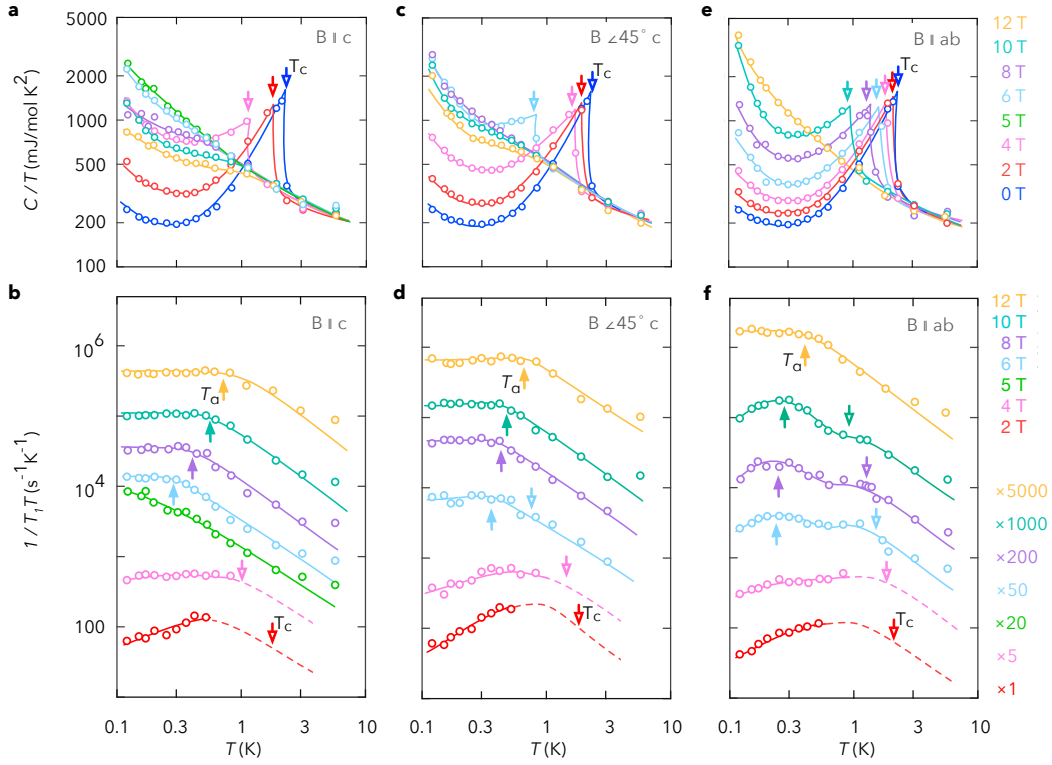


FIG. 2 **Temperature dependence of  $C/T$  and  $1/T_1T$ .** **a,c,e.**  $C/T$  shown for three orientations of the magnetic field,  $B \parallel c$ ,  $B \angle 45^\circ c$ , and  $B \parallel ab$  with magnetic fields from 0 to 12 T. Open (downward) arrows denote the superconducting transition at  $T_c(B, \theta)$ , corresponding to upper critical field  $B_{c2}(T) = B$ . (See also Figure S4.) **b,d,f.** Corresponding  $1/T_1T$  for magnetic fields from 2 to 12 T, shifted vertically for clarity (the shift factors are indicated in the legend, unshifted curves are shown in Figure E2). Filled (upward) arrows denote the crossover temperature scale  $T_a(B, \theta)$ . Open (downward) arrows denote the superconducting transition  $T_c(B, \theta)$  from the corresponding panels a,c,e. The solid curves are guides for the eye. Corresponding nuclear specific heat is shown in Figure E3.

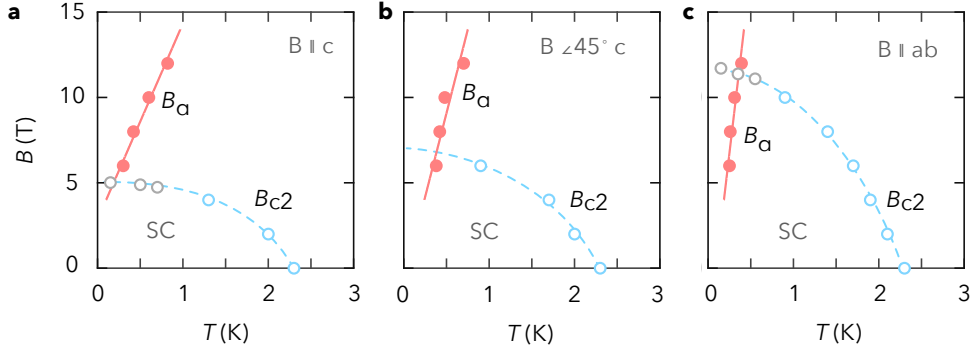


FIG. 3 **Crossover field and superconducting phase boundary.** **a,b,c.** Temperature dependence of the crossover field  $B_\alpha(T, \theta)$  for three orientations (filled red circles) determined from Figure 2b,d,f. Open blue markers represent  $B_{c2}(T, \theta)$  determined from Figure 2a,c,e. Open grey markers represent AC-calorimetry measurements (see Figure E1). Solid lines and dashed curves are guides for the eye. See also Figure S4.

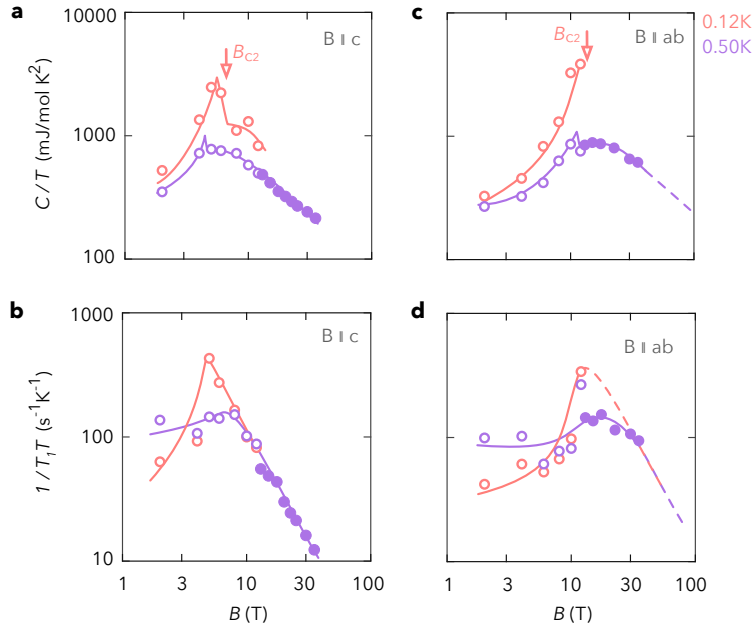


FIG. 4 **Electronic  $C/T$  and  $1/T_1T$  at high magnetic fields.** **a,c.** Magnetic field dependence of  $C/T$  for field along the  $c$ -axis and parallel to the  $ab$ -plane at two temperatures, 0.12 K and 0.5 K. Open markers correspond to magnetic field slices in Figure 2a,c,e. Filled markers represent high-field measurements up to 35 T. Dashed curves represent the high-field behavior expected from field along the  $c$ -axis (panel a). Solid curves are guides for the eye. **b,d.** Corresponding  $1/T_1T$ .

## 4. METHODS

### A. Sample characterization and preparation

CeCoIn<sub>5</sub> has tetragonal crystal structure with a unit cell described by lattice parameters  $a = b = 4.61 \text{ \AA}$  and  $c = 7.55 \text{ \AA}$ , containing one formula unit (51). The molar (as well as f.u.) volume of CeCoIn<sub>5</sub> is  $96.6 \text{ cm}^3/\text{mol}$ , the molar mass  $140 + 59 + 115 \times 5 = 774 \text{ g/mol}$  and mass-density (51) is  $8.04 \text{ g/cm}^3$ . A CeCoIn<sub>5</sub> single crystal was cleaved into an approximately cuboid shape of dimensions  $50(2) \times 25(2) \times 20(2) \text{ }\mu\text{m}^3$  ( $0.25 \text{ nmol(f.u)}$  or  $0.20 \text{ }\mu\text{g}$  mass). The sample mass estimate was checked to be within the approximately 10% spread of specific heat measurements in References [52–57] over the temperature range from 0.6 K to 2 K (see Figure S1). The sample was mounted on a calorimeter platform (30; 58; 59) using a thin layer of Apiezon-N grease.

### B. Measurements of thermal impedance spectra

Thermal impedance spectra were measured over a  $f = 10 \text{ mHz} - 5 \text{ kHz}$  frequency range using a multi-channel lock-in technique. The sample temperature was controlled using an offset heater lithographically defined in the nanocalorimeter (58; 59). A superimposed temperature oscillation at frequency  $f$  was generated by a current at frequency  $f/2$  on a separate AC-heater defined lithographically in good thermal contact with the calorimeter platform (see Figure M1). The thin-film thermometer (60) was DC-biased with a  $100 \text{ k}\Omega$  series resistor, resulting in complex (in-phase, out-of-phase) thermometer voltage oscillation at frequency  $f$ , translated into a complex calorimeter platform temperature oscillation amplitude  $T^{\text{C}}(f)$  using a thermometer calibration function. The thermal impedance of the calorimeter-sample assembly  $\zeta(f)$  was obtained by dividing  $T^{\text{C}}(f)$  by the power  $P(f)$  of the AC-heater,

$$\zeta(\omega) = T^{\text{C}}(\omega)/P(\omega) \quad (\text{M1})$$

where  $\omega = 2\pi f$  is the angular frequency. An example of the thermal impedance spectra with corresponding fits is shown in Figure E6. Further measurements of thermal impedance spectra are shown in Figure E7.

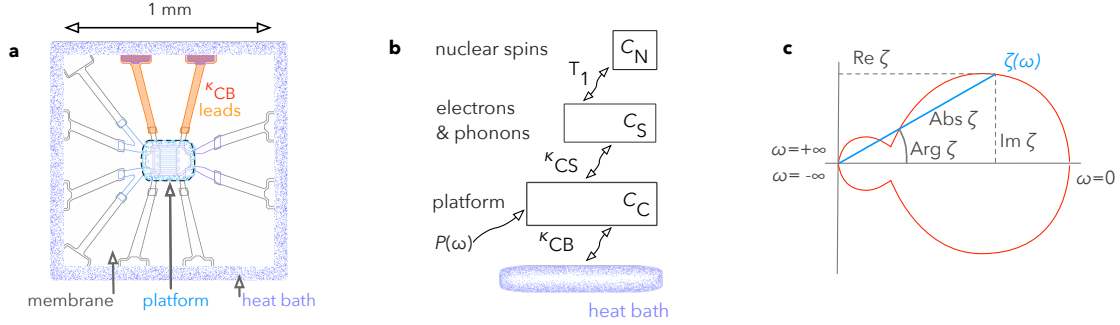


FIG. M1 **Thermal impedance spectroscopy of CeCoIn<sub>5</sub>.** **a.** Sketch of lithographically defined nanocalorimeter showing its major components; thermal bath (280  $\mu\text{m}$  silicon wafer, in purple), calorimeter platform containing thermometer and heater (in blue), the thermally insulating membrane (150 nm  $\text{SiN}_x$ ), and gold-capped chromium leads (about 60 nm thick) (30; 58; 59). **b.** Heat flow diagram of the calorimeter-sample assembly that underlies the thermal impedance of equation (M2). The nuclear-spin subsystem represents indium and cobalt nuclei. **c.** Definition of polar and vector components of the thermal impedance in the complex plane.

### C. Heat-flow model of the calorimeter-sample assembly

The thermal circuit in Figure M1b is modeled by the thermal impedance  $\zeta(\omega)$  given by

$$\frac{1}{\zeta(\omega)_{\text{model}}} = \kappa_{CB} - i\omega C_C + \frac{-i\omega \left( C_S + \frac{C_N}{-i\omega T_1 + 1} \right) \kappa_{CS}}{-i\omega \left( C_S + \frac{C_N}{-i\omega T_1 + 1} \right) + \kappa_{CS}}, \quad (\text{M2})$$

where  $\kappa_{CB}$  is the thermal conductance of the thermal link (shown in orange in Figure M1a) between the calorimeter platform (blue) to the heat bath (purple).  $\kappa_{CS}$  is the thermal link between the sample and the calorimeter platform;  $C_S$  is the heat capacity of the sample (excluding the nuclear heat capacity),  $C_N$  is the nuclear heat capacity, and  $C_C$  is the heat capacity of the calorimeter platform, respectively.  $T_1$  is the nuclear spin-lattice relaxation time.

#### D. Fitting of thermal impedance spectra

Fitting of the observed thermal impedance spectra to the model are done using gradient descent minimization of the goodness function

$$g(\{\lambda_i\})_{\beta(\omega)} = \int d\omega \beta(\omega) \times \left[ \zeta(\omega)^{\text{obs}} - \zeta(\omega)_{\{\lambda_i\}}^{\text{model}} \right]^* \times \left[ \zeta(\omega)^{\text{obs}} - \zeta(\omega)_{\{\lambda_i\}}^{\text{model}} \right] \quad (\text{M3})$$

where  $\beta(\omega)$  is a weighting function and  $\lambda_{i=1..6}$  are six parameters for  $\zeta(\omega)^{\text{model}}$  in equation (M2) as described above. The fitting was done using custom software. The error bars for the fitting parameters were estimated from the analysis of the curvature of the goodness function of equation (M3) as described in Reference [30].

All Figures in the main text represent the results of unconstrained six-parameter fits. We checked that three of the fitting parameters,  $\kappa_{\text{CS}}$  (calorimeter-sample thermal link),  $\kappa_{\text{CB}}$  (calorimeter-bath thermal link), and  $C_C$  (calorimeter heat capacity), are consistent across all fits.

#### Acknowledgments

A.K. and A.R. acknowledge support from the Swedish Research Council, D. Nr. 2021-04360. Resistive 35 T magnet measurements were performed at the National High Magnetic Field Laboratory, which is supported by the National Science Foundation Cooperative Agreement No. DMR-1644779 and DMR-2128556 and the State of Florida. Work at Los Alamos National Laboratory is supported by the NSF through DMR-1644779 and DMR-2128556 and the U.S. Department of Energy. A.S. acknowledges support from the DOE/BES ‘‘Science of 100 T’’ grant. A.S. acknowledges the hospitality of the Aspen Center for Physics, where part of the data analysis was performed. Aspen Center for Physics is supported by National Science Foundation grant No. PHY-1607611. We thank A. Thamizhavel for providing single crystals of  $\text{CeCoIn}_5$ . We thank Kim Schneider for help with image editing.

#### References

- [1] C. Petrovic, P. Pagliuso, M. Hundley, R. Movshovich, J. Sarrao, J. Thompson, Z. Fisk, and P. Monthoux, *Journal of Physics: Condensed Matter* **13**, L337 (2001).

- [2] L. Pham, T. Park, S. Maquilon, J. Thompson, and Z. Fisk, *Phys. Rev. Lett.* **97**, 056404 (2006).
- [3] E. D. Bauer, F. Ronning, C. Capan, M. J. Graf, D. Vandervelde, H. Q. Yuan, M. B. Salamon, D. J. Mixson, N. O. Moreno, S. R. Brown, J. D. Thompson, R. Movshovich, M. F. Hundley, J. L. Sarrao, P. G. Pagliuso, and S. M. Kauzlarich, *Physical Review B* **73**, 245109 (2006).
- [4] M. Nicklas, O. Stockert, T. Park, K. Habicht, K. Kiefer, L. D. Pham, J. D. Thompson, Z. Fisk, and F. Steglich, *Physical Review B* **76**, 052401 (2007).
- [5] S. M. Ramos, M. B. Fontes, E. N. Hering, M. A. Continentino, E. Baggio-Saitovich, F. D. la Neto, E. M. Bittar, P. G. Pagliuso, E. D. Bauer, J. L. Sarrao, and J. D. Thompson, *Physical Review Letters* **105**, 126401 (2010).
- [6] R. Settai, H. Shishido, S. Ikeda, Y. Murakawa, M. Nakashima, D. Aoki, Y. Haga, H. Harima, and Y. Onuki, *Journal of Physics: Condensed Matter* **13**, L627 (2001).
- [7] A. Bianchi, R. Movshovich, I. Vekhter, P. Pagliuso, and J. Sarrao, *Phys. Rev. Lett.* **91**, 257001 (2003).
- [8] F. Ronning, C. Capan, A. Bianchi, R. Movshovich, A. Lacerda, M. Hundley, J. Thompson, P. Pagliuso, and J. Sarrao, *Physical Review B* **71**, 104528 (2005).
- [9] M. Yokoyama, K. Suzuki, K. Tenya, S. Nakamura, Y. Kono, S. Kittaka, and T. Sakakibara, *Physical Review B* **99**, 054506 (2019).
- [10] Y. Kohori, Y. Yamato, Y. Iwamoto, T. Kohara, E. D. Bauer, M. B. Maple, and J. L. Sarrao, *Physical Review B* **64**, 134526 (2001).
- [11] Y. Kawasaki, S. Kawasaki, M. Yashima, T. Mito, G. qing Zheng, Y. Kitaoka, H. Shishido, R. Settai, Y. Haga, and Y. Onuki, *Journal of the Physical Society of Japan* **72**, 2308 (2003).
- [12] N. Curro and D. Pines, *Journal of Physics and Chemistry of Solids* **68**, 2028 (2007).
- [13] H. Sakai, S. E. B. Seung-Ho Baek, F. Ronning, E. D. Bauer, and J. D. Thompson, *Phys. Rev. B* **82**, 020501(R) (2010).
- [14] H. Sakai, S. Brown, S.-H. Baek, F. Ronning, E. Bauer, and J. Thompson, *Phys. Rev. Lett.* **107**, 137001 (2011).
- [15] M. Yamashita, M. Tashiro, K. Saiki, S. Yamada, M. Akazawa, M. Shimozawa, T. Taniguchi, H. Takeda, M. Takigawa, and H. Shishido, *Physical Review B* **102**, 165154 (2020).
- [16] H. Sakai, Y. Tokunaga, S. Kambe, J.-X. Zhu, F. Ronning, J. D. Thompson, S. K. Ramakrishna, A. P. Reyes, K. Suzuki, Y. Oshima, and M. Yokoyama, *Phys. Rev. B* **104**, 085106 (2021).

- [17] G. R. Stewart, *Rev. Mod. Phys.* **73**, 797 (2001).
- [18] H. V. Lohneysen, A. Rosch, M. Vojta, and P. Wolfle, *Rev. Mod. Phys.* **79**, 1015 (2007).
- [19] P. Gegenwart, Q. Si, and F. Steglich, *Nature Physics* **4**, 186 (2008).
- [20] Q. Si and F. Steglich, *Science* **329**, 1161 (2010).
- [21] J. Custers, P. Gegenwart, H. Wilhelm, K. Neumaier, Y. Tokiwa, O. Trovarelli, C. Geibel, F. Steglich, C. Pepin, and P. Coleman, *Nature* **424**, 524 (2003).
- [22] Y. Nakajima, K. Izawa, Y. Matsuda, S. Uji, T. Terashima, H. Shishido, R. Settai, Y. Onuki, and H. Kontani, *Journal of the Physical Society of Japan* **73**, 5 (2004).
- [23] P. W. Anderson, *Science* **256**, 1526 (1992).
- [24] B. Keimer, S. A. Kivelson, M. R. Norman, S. Uchida, and J. Zaanen, *Nature* **518**, 179 (2015).
- [25] J. Paglione, M. A. Tanatar, D. G. Hawthorn, E. Boaknin, R. Hill, F. Ronning, M. Sutherland, and L. Taillefer, *Phys. Rev. Lett.* **91**, 246405 (2003).
- [26] J. Paglione, M. Tanatar, D. Hawthorn, F. Ronning, R. Hill, M. Sutherland, L. Taillefer, and C. Petrovic, *Phys. Rev. Lett.* **97**, 106606 (2006).
- [27] A. Malinowski, M. F. Hundley, C. Capan, F. Ronning, R. Movshovich, N. O. Moreno, J. L. Sarrao, and J. D. Thompson, *Physical Review B* **72**, 184506 (2005).
- [28] Y. Tokiwa, P. Gegenwart, and E. D. Bauer, *Phys. Rev. Lett.* **111**, 107003 (2013).
- [29] P. Giraldo-Gallo, J. A. Galvis, Z. Stegen, K. A. Modic, F. F. Balakirev, J. B. Betts, X. Lian, C. Moir, S. C. Riggs, J. Wu, A. T. Bollinger, X. He, I. Bozovic, B. J. Ramshaw, R. D. McDonald, G. S. Boebinger, and A. Shekhter, *Science* **361**, 479 (2018).
- [30] A. Khansili, A. Bangura, R. D. McDonald, B. J. Ramshaw, A. Rydh, and A. Shekhter, *Phys. Rev. B* **127**, 195145 (2023).
- [31] J. Korrying, *Physica* **16**, 601 (1950).
- [32] A. Abragam, *The principles of nuclear magnetism* (Oxford university press, 1961).
- [33] L. D. Landau, *Sov. Phys. JETP* **3**, 920 (1957).
- [34] A. Ishigaki and T. Moriya, *Journal of the Physical Society of Japan* **65**, 3402 (1996).
- [35] T. Moriya and K. Ueda, *Advances in Physics* **49**, 555 (2000).
- [36] T. Moriya, *Journal of the Physical Society of Japan* **18**, 516 (1963).
- [37] L. D. Landau, E. M. Lifshitz, and L. Pitaevskii, *Course of Theoretical Physics Vol 9 : Statistical Physics, Part 2 : by E.M. Lifshitz and L.P. Pitaevskii* (Pergamon Press, 1980).
- [38] A. Abrikosov, *Fundamentals of the Theory of Metals* (Dover Publications, 2017).

- [39] H. Shishido, S. Yamada, K. Sugii, M. Shimozawa, Y. Yanase, and M. Yamashita, *Phys. Rev. Lett.* **120**, 177201 (2018).
- [40] N. Maksimovic, D. H. Eilbott, T. Cookmeyer, F. Wan, J. Rusz, V. Nagarajan, S. C. Haley, E. Maniv, A. Gong, S. Faubel, I. M. Hayes, A. Bangura, J. Singleton, J. C. Palmstrom, L. Winter, R. McDonald, S. Jang, P. Ai, Y. Lin, S. Ciocys, J. Gobbo, Y. Werman, P. M. Oppeneer, E. Altman, A. Lanzara, and J. G. Analytis, *Science* **375**, 76 (2022).
- [41] J. Bardeen, L. N. Cooper, and J. R. Schrieffer, *Physical Review* **108**, 1175 (1957).
- [42] M. Yashima, S. Kawasaki, Y. Kawasaki, G. q. Zheng, Y. Kitaoka, H. Shishido, R. Settai, Y. Haga, and Y. Onuki, *journal of the physical society of japan* **73**, 2073 (2004).
- [43] B. Ramshaw, A. Shekhter, R. McDonald, J. Betts, J. Mitchell, P. Tobash, C. Mielke, E. Bauer, and A. Migliori, *PNAS* **112**, 3285 (2015).
- [44] P. W. Anderson and W. F. Brinkman, *Phys. Rev. Lett.* **30**, 1108 (1973).
- [45] A. J. Leggett, *Rev. Mod. Phys.* **47**, 331 (1975).
- [46] P.-G. de Gennes, *Superconductivity of metals and alloys* (Avalon Publishing, 1999).
- [47] G. E. Volovik and V. P. Mineev, *JETP Lett.* **24**, 561 (1976).
- [48] N. B. Kopnin and M. M. Salomaa, *Phys. Rev. B* **44**, 9667 (1991).
- [49] H. B. Callen, *Thermodynamics and an Introduction to Thermostatistics* (Wiley & Sons, 1985).
- [50] A. J. Leggett, *Phys. Rev. Lett.* **29**, 1227 (1972).
- [51] E. Moshopoulou, J. Sarrao, P. Pagliuso, N. Moreno, J. Thompson, Z. Fisk, and R. Ibberson, *Applied Physics A* **74**, s895 (2002).
- [52] R. Movshovich, M. Jaime, J. Thompson, C. Petrovic, Z. Fisk, P. Pagliuso, and J. Sarrao, *Phys. Rev. Lett.* **86**, 5152 (2001).
- [53] S. Ikeda, H. Shishido, M. Nakashima, R. Settai, D. Aoki, Y. Haga, H. Harima, Y. Aoki, T. Namiki, H. Sato, and Y. Onuki, *Journal of the Physical Society of Japan* **70**, 2248 (2001).
- [54] G. Sparn, R. Borth, E. Lengyel, P. Pagliuso, J. Sarrao, F. Steglich, and J. Thompson, *Physica B: Condensed Matter* **319**, 262 (2002).
- [55] K. An, T. Sakakibara, R. Settai, Y. Onuki, M. Hiragi, M. Ichioka, and K. Machida, *Phys. Rev. Lett.* **104**, 037002 (2010).
- [56] J. Kim, D. Bedorf, and G. Stewart, *Journal of Low Temperature Physics* **157**, 29 (2009).
- [57] E. Lengyel, R. Borth, P. Pagliuso, J. Sarrao, G. Sparn, F. Steglich, and J. Thompson, *High Pressure Research* **22**, 185 (2002).



- [58] S. Tagliati, V. M. Krasnov, and A. Rydh, *Review of Scientific Instruments* **83**, 055107 (2012).
- [59] K. Willa, Z. Diao, D. Campanini, U. Welp, R. Divan, M. Hudl, Z. Islam, W.-K. Kwok, and A. Rydh, *Review of Scientific Instruments* **88**, 125108 (2017).
- [60] N. A. Fortune, J. E. Palmer-Fortune, A. Trainer, A. Bangura, N. Kondedan, and A. Rydh, *Phys. Rev. Applied* **20**, 054016 (2023).
- [61] L. C. Hebel, *Solid State Physics* **15**, 409 (1963).
- [62] N. J. Stone, INDC, International Nuclear Data Committee INDC **(NDS)-0658 Distr** (2014).

## 5. SUPPLEMENTARY INFORMATION

### A. AC calorimetry data

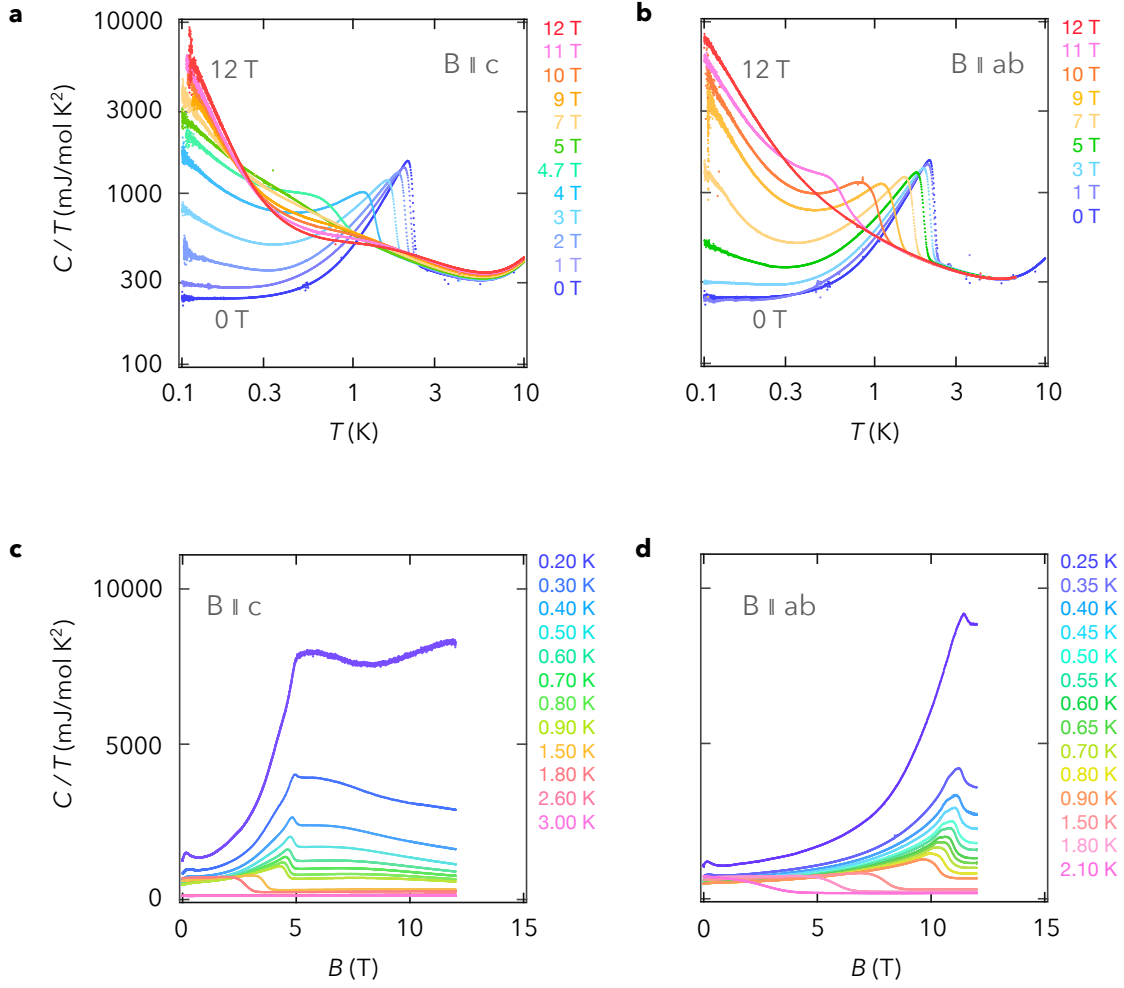


FIG. E1 **AC calorimetry data.** **a,b.** Specific heat for different magnetic fields applied along the  $c$ -axis and  $ab$ -plane, respectively, for a 0.50 nmol sample. **c,d.** Magnetic field dependence of the specific heat.

## B. Temperature dependence of $1/T_1T$

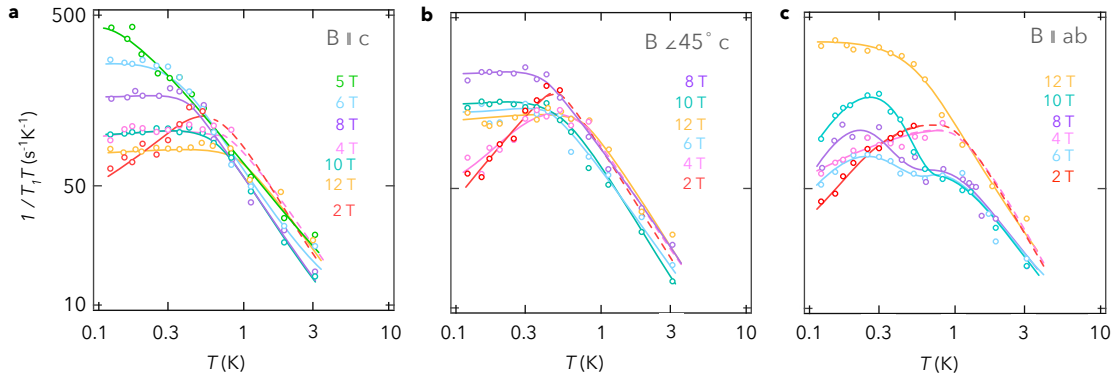


FIG. E2 **Temperature dependence of  $1/T_1T$ .** Nuclear spin-lattice relaxation rate in Figure 2b,d,f in the main text, shown here without vertical offset. All lines are guides to the eye.

### C. Nuclear specific heat

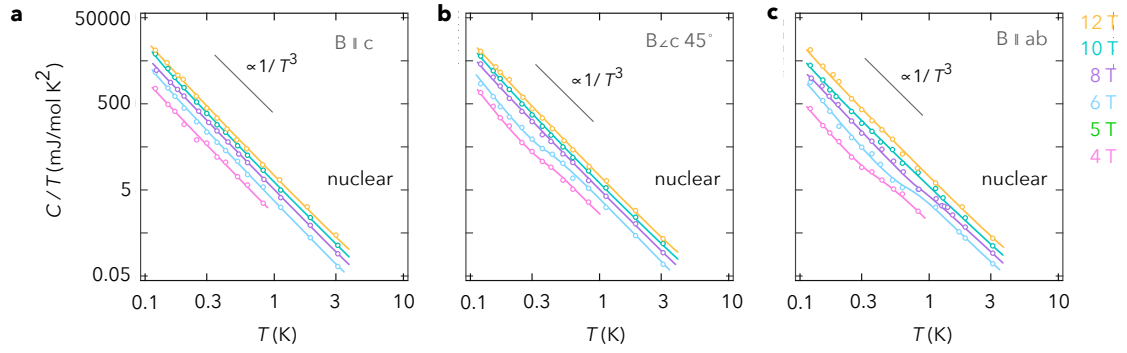


FIG. E3 **Nuclear specific heat.** **a,b,c.** Nuclear specific heat shown as  $C_N/T$  for different magnetic fields and magnetic field orientations. All solid curves are guides for the eye.

### D. Entropy for some magnetic fields and field orientations

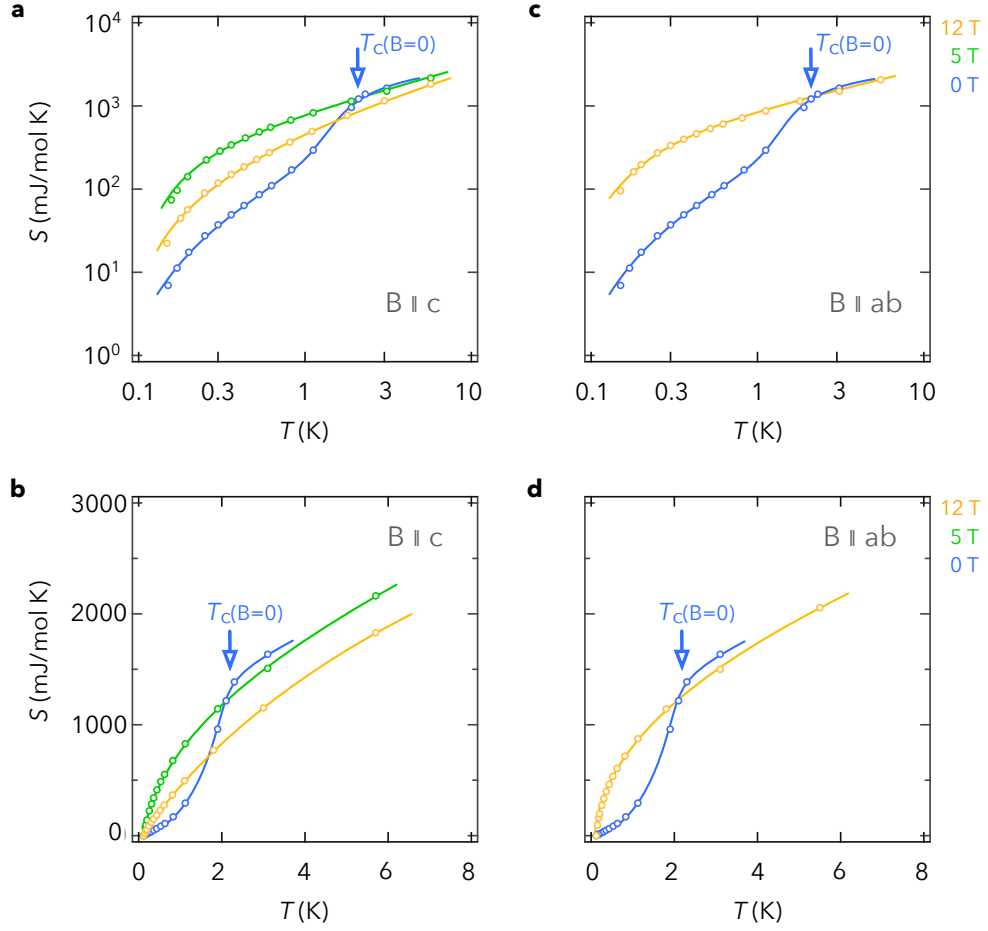


FIG. E4 Entropy for some magnetic fields and field orientations. **a,b.** Entropy as a function of temperature for  $B \parallel c$  in log-log scale (panel a) and lin-lin scale (panel b). **c,d.** Corresponding entropy for  $B \parallel ab$ . The full set of magnetic fields are shown in Figure E5.

### E. Entropy for several magnetic fields and field orientations

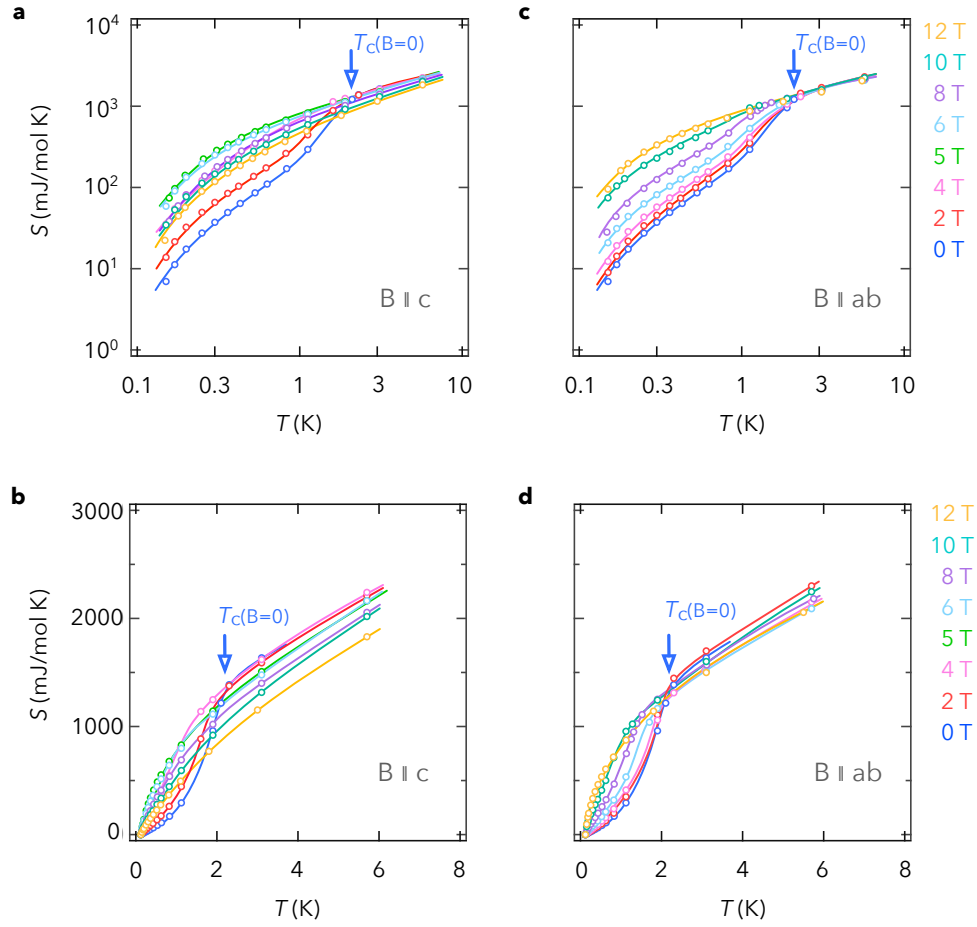


FIG. E5 **Entropy for several magnetic fields and field orientations.** Entropy as described in Figure E4, for the full set of magnetic fields.

## F. Thermal impedance data

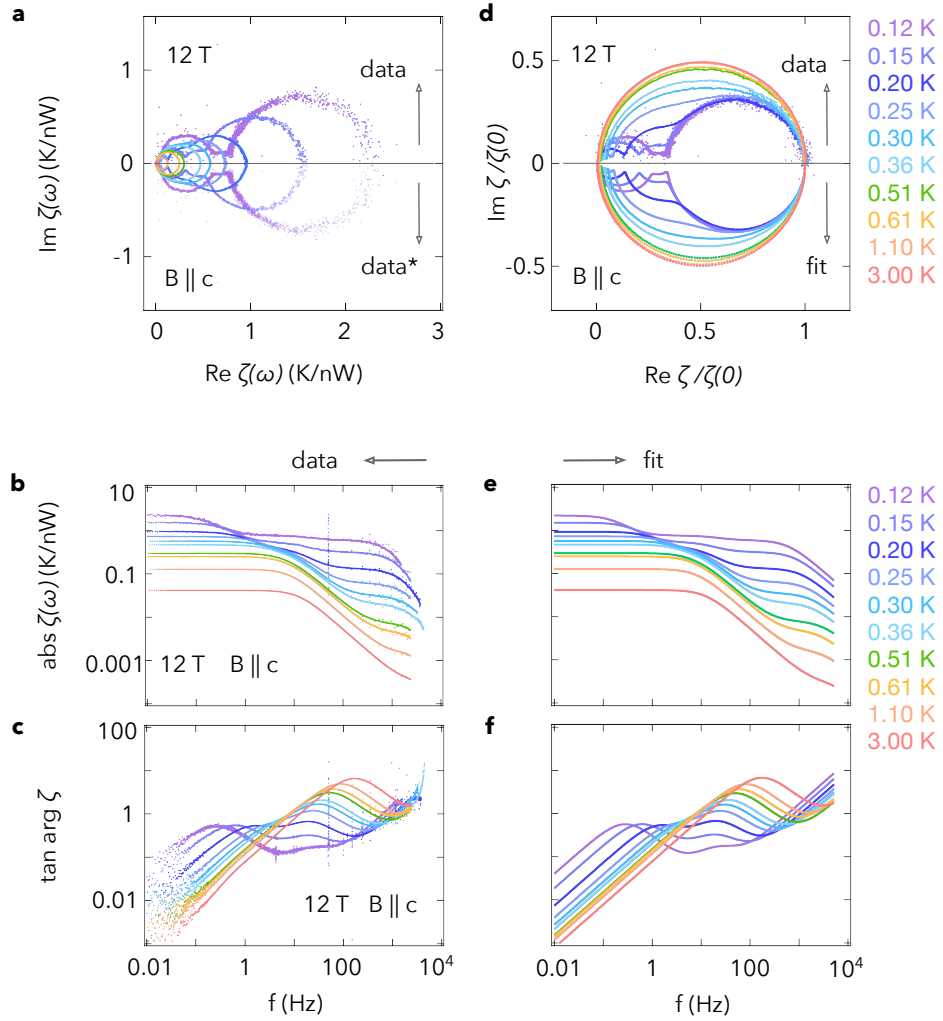
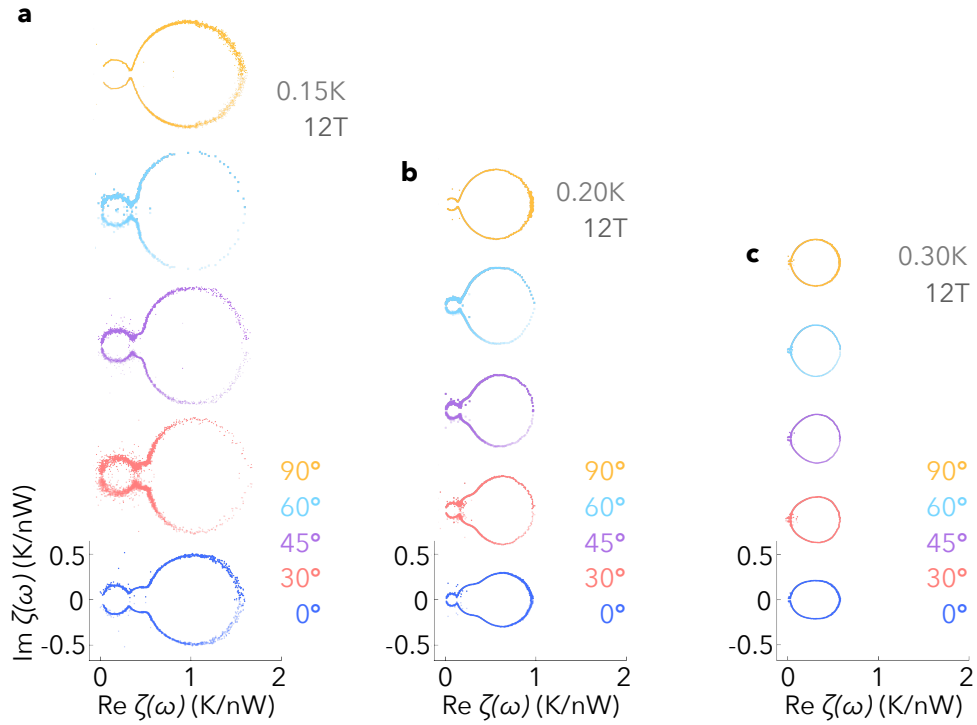


FIG. E6 **Thermal impedance data.** **a.** Thermal impedance at 12 T along the  $c$ -axis, for temperatures from 0.12 K to 3 K. The upper half  $\text{Im}\zeta(\omega) > 0$ , shows the observed thermal impedance. The lower half  $\text{Im}\zeta(\omega) < 0$ , is "mirrored" as a guide for the eye,  $\zeta(-\omega) = \zeta^*(\omega)$ . **b,c.** Frequency dependence of the polar components (amplitude and phase) of the observed thermal impedance in the range 10 mHz to 5 kHz. **d.** Normalized thermal impedance  $\zeta(\omega)/\zeta(\omega = 0)$ . The lower half shows the result of the fit to equation (M2). **e,f.** Corresponding frequency dependences of the polar components for the fits to the model.

**G. Thermal impedance spectra for different temperatures and magnetic field orientations**



**FIG. E7 Thermal impedance spectra for different temperatures and magnetic field orientations.** **a,b,c.** Thermal impedance spectra of the calorimeter-sample assembly at 12 T for a frequency range of 10 mHz to 5 kHz for a set of angles at 0.15 K, 0.20 K, and 0.30 K, respectively, shown here in the complex plane of  $\zeta(\omega)$ . Each spectrum gives one data point in Figure 1e,f,g of the main text. The "multi-circle" geometry indicates directly the multi-relaxation time character of the thermal impedance.



## H. Comparison of zero field $C/T$

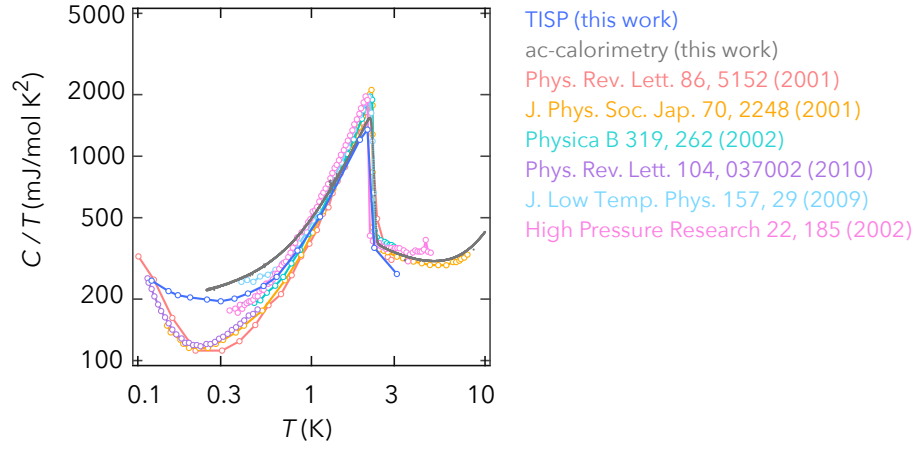


FIG. S1 **Comparison of  $C/T$  of  $\text{CeCoIn}_5$  at zero field.** Measurements in this work (TISP: open blue circles, AC calorimetry: black dots) are compared with measurements from References [52–57]. Over the temperature range of 0.6 K to 2 K, all measurements fall within 10% of each other.

### I. Evaluation of $T_\alpha$ at 12 T

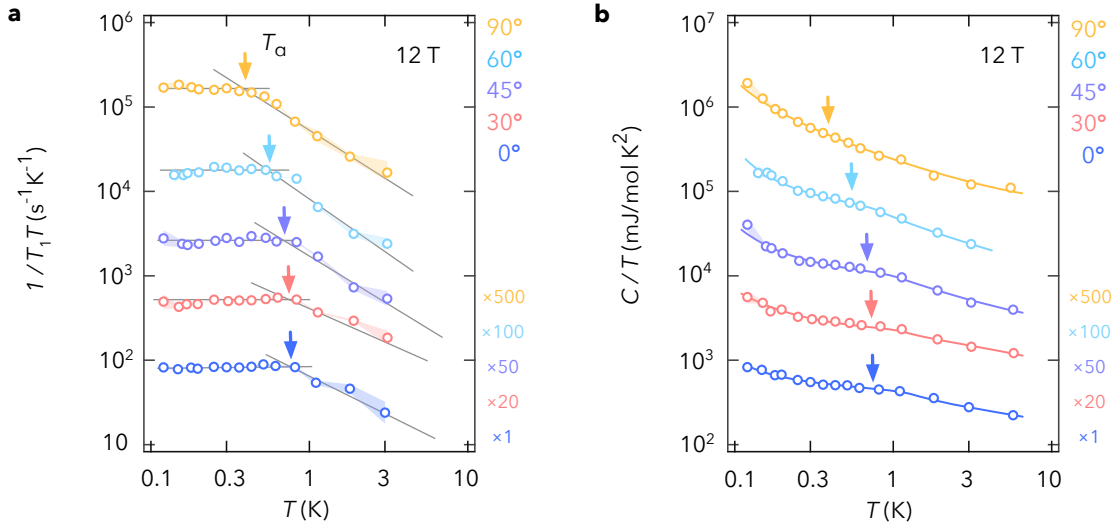


FIG. S2 **Evaluation of  $T_\alpha$  at 12 T.** **a.**  $1/T_1 T$  in Figure 1e in the main text, shifted vertically to highlight the crossover region for each temperature sweep. Thin gray lines indicate the limiting behavior below and above crossover  $T_\alpha$ . The value of  $T_\alpha$  is determined as the crossing point of the two gray lines, as indicated by the arrow. **b.**  $C/T$  in Figure 1f in the main text shifted vertically for clarity. The location of  $T_\alpha$ , as determined by analysis of  $1/T_1 T$  in panel a, are shown as arrows.

### J. Evaluation of $T_\alpha$ and $T_c$ for different magnetic fields and field orientations

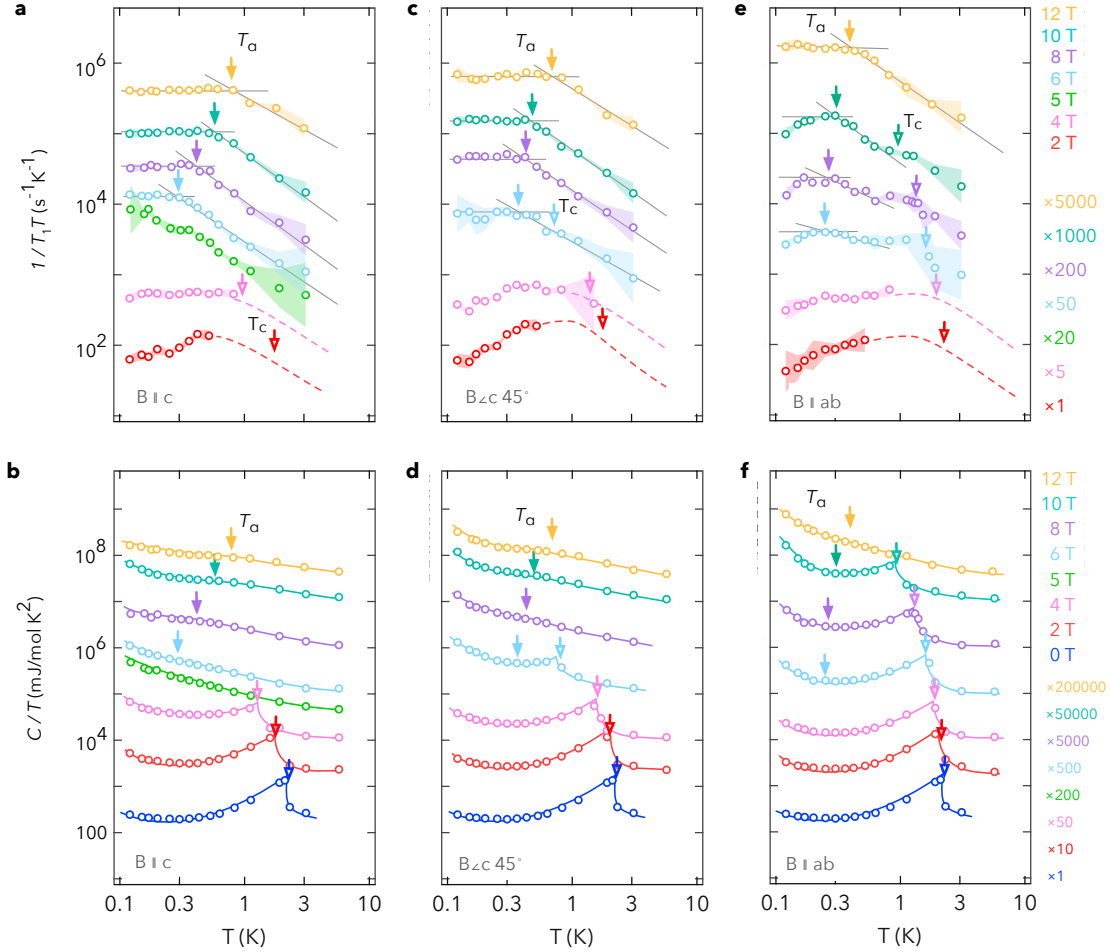


FIG. S3 Evaluation of  $T_\alpha$  and  $T_c$  for different orientations and magnitudes of magnetic fields. **a,c,e.** Temperature dependence of  $1/T_1T$  from Figure 2 in the main text at different magnetic fields, offset vertically for clarity. Solid gray lines indicate the limiting behavior above and below the crossover temperature  $T_\alpha$ , similar to Figure S2. The crossover temperature  $T_\alpha$  is determined as their intercept, indicated by the solid arrow. The color shading indicates the fitting error bars as described in Section 4. **b,d,f.** Corresponding specific heat of Figure 2 of the main text. The open arrows indicate the superconducting transition temperature.  $T_\alpha$ , as determined from  $1/T_1T$ , are shown as solid arrows.

**K. Magnetic field dependence of  $T_\alpha(B)$  and  $T_c(B)$**

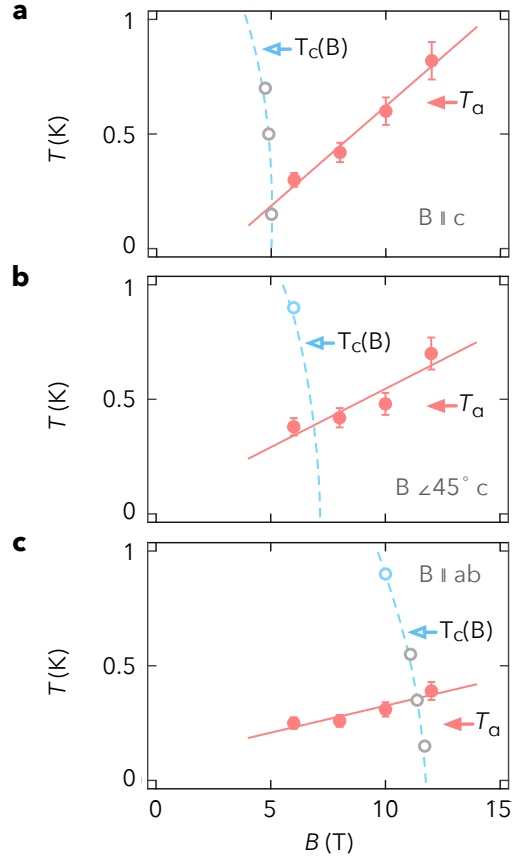


FIG. S4 **Magnetic field dependence of  $T_\alpha$  and  $T_c(B)$ .** **a,b,c.** Magnetic field dependence of  $T_\alpha(B)$  and  $T_c(B)$  for magnetic fields along the  $c$ -axis, at  $B \angle 45^\circ$ , and along the  $ab$ -plane, respectively. See also Figure 3 of the main text.

## L. Determination of $q$ -factors

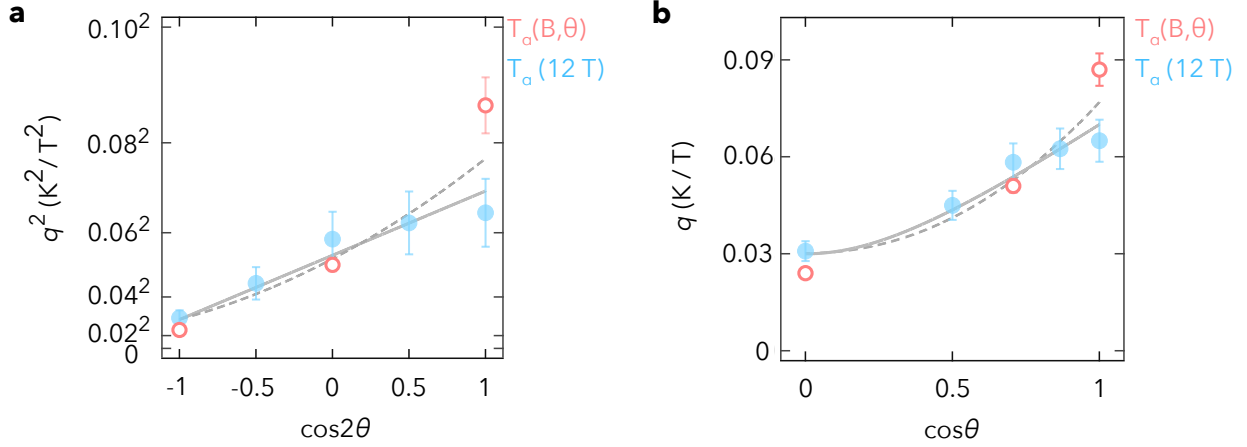


FIG. S5 **Determination of  $q$ -factors.** **a.** Angular dependence of  $q^2(\theta)$  vs  $\cos 2\theta$  determined as  $q^2(\theta) = (T_\alpha/B)^2$  in Figure S2 and from the slopes in Figure S4 using  $q^2(\theta) \approx (dT_\alpha/dB)^2$ . The approximate linear dependence is consistent with lowest-angular-harmonic behavior of the tetragonal lattice structure of  $\text{CeCoIn}_5$ ,  $q^2(\theta) = q_c^2 \cos^2 \theta + q_{ab}^2 \sin^2 \theta$ , or, equivalently  $q^2(\theta) = 1/2(q_c^2 + q_{ab}^2) + 1/2(q_c^2 - q_{ab}^2) \cos 2\theta$ . The linear regression of the data in panel a produces  $1/2(q_c^2 + q_{ab}^2) = 2.9(5) (\text{mK}/\text{T})^2$  and  $1/2(q_c^2 - q_{ab}^2) = 2.0(2) (\text{mK}/\text{T})^2$ . This corresponds to  $q_c = 70(5) \text{ mK}/\text{T}$  and  $q_{ab} = 30(5) \text{ mK}/\text{T}$ . The solid line represents the linear fit. The dotted curve corresponds to the best-fit with the second and fourth harmonics,  $q^2(\theta) = a + b \cos 2\theta + c \cos 4\theta$  with parameters  $a = 3.1(5) (\text{mK}/\text{T})^2$ ,  $b = 2.5(2) (\text{mK}/\text{T})^2$ , and  $c = 0.30(2) (\text{mK}/\text{T})^2$ . Such higher order harmonic fit changes the values of the  $q$ -factors to  $q_c = 75(5) \text{ mK}/\text{T}$  and  $q_{ab} = 25(5) \text{ mK}/\text{T}$ . **b.**  $q(\theta)$  plotted vs  $\cos \theta$ . Solid curve represents the lowest harmonic approximation,  $q(\theta) = (q_c^2 \cos^2 \theta + q_{ab}^2 \sin^2 \theta)^{1/2}$  with  $q_c$  and  $q_{ab}$  determined by linear regression in panel a. The dotted curve represents the the best-fit for the fourth harmonic approximation.

### M. Normalized $C/T$ for different magnetic fields and field orientations

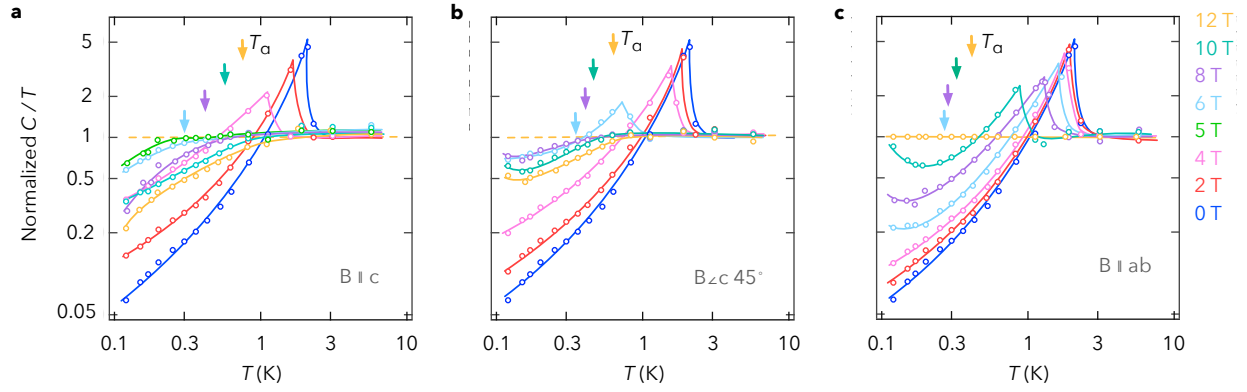


FIG. S6 Normalized  $C/T$  for different magnetic fields and field orientations. **a,b,c.** Electronic  $C/T$  divided by  $C/T$  at 12 T along the  $ab$ -plane in the normal state. The arrows represent the crossover temperature  $T_\alpha(B)$  determined in Figure S3.

## N. Two nuclear components in CeCoIn<sub>5</sub>

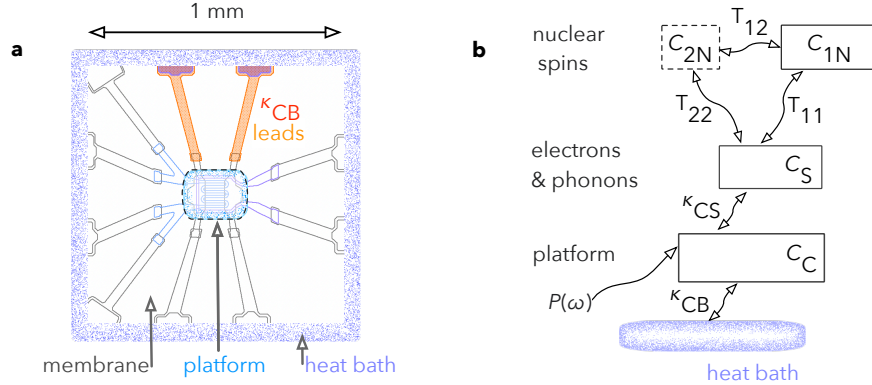


FIG. S7 **Heat flow diagram of the calorimeter-sample assembly with two nuclear components.** **a.** A sketch of the calorimeter, indicating different components. **b.** Heat flow diagram of the calorimeter-sample assembly which determines the thermal impedance in equation (S1). CeCoIn<sub>5</sub> has two nuclear spin subsystems, that of <sup>115/113</sup>In ( $C_{1N}$ ) and that of <sup>59</sup>Co ( $C_{2N}$ ).

The model described in Section 4 accounts for a single nuclear isotope species coupled to the electrons via the nuclear spin lattice relaxation rate  $1/T_1$ . In CeCoIn<sub>5</sub>, about 13% of the nuclear heat capacity comes from <sup>59</sup>Co while the rest comes from <sup>115/113</sup>In. The resulting two-nuclear-component heat circuit is described by a larger (9-parameter) model,

$$\frac{1}{\zeta(\omega)_2^{\text{model}}} = \kappa_{CB} - i\omega C_C + \frac{-i\omega \left( C_S + \frac{C_{1N}}{-i\omega T_{11} + 1} + \frac{C_{2N}}{-i\omega T_{22} + 1} \right) \kappa_{CS}}{-i\omega \left( C_S + \frac{C_{1N}}{-i\omega T_{11} + 1} + \frac{C_{2N}}{-i\omega T_{22} + 1} \right) + \kappa_{CS}}, \quad (\text{S1})$$

where  $T_{11}$  and  $T_{22}$  are the spin-lattice relaxation times for In and Co, respectively. We have assumed that the cross-relaxation rate  $1/T_{12}$  [32; 61] is zero.

Detailed investigation of the two-component nuclear specific heat as well as effects of cross-relaxation is beyond the scope of this work. We now show that in TISP measurements, inclusion of these effects does not affect the magnitude of the electronic specific heat and the nuclear spin-lattice relaxation rates at the level of accuracy necessary for the discussion in the main text.

The weak sensitivity of the magnitude of  $C_S$  and  $T_1$  to changes in the nuclear system is rooted in the fact that in TISP measurements, the nuclear specific heat  $C_N$  and the electronic specific heat  $C_S$  are determined independently by the frequency-dependent thermal impedance. For example, *if* the calorimeter-sample assembly is described by the single-isotope thermal impedance (equation (M2) in Section 4), then *any* changes in the magnitude

of the nuclear specific heat  $C_N$  have *zero* effect on the magnitude of all other parameters, including that of  $C_S$  and  $T_1$ .

As a consequence of such "robustness", even when we modify the nuclear subsystem in a more significant way, such as the two-isotope (equation (S1)) versus single-isotope (equation (M2) in Section 4), the differences in the values of  $C_S$  and  $T_1$  determined from fits to the two models are parametrically smaller than the differences in the parameters of the nuclear subsystem, as long as the latter are relatively small (see Supplementary Note 3 for mathematical details).

Specifically, for  $\text{CeCoIn}_5$ , the nuclear specific heat consists of 13%  $^{59}\text{Co}$  and 87%  $^{113/115}\text{In}$  and the nuclear spin-lattice relaxation rate of  $^{59}\text{Co}$  is about five times smaller than that of  $^{115/113}\text{In}$  (Figure S8) [14; 42]. The relatively small, 13% "redistribution" of the nuclear specific heat components in equation (S1) has much smaller, less than 1%, effect on the magnitude of the electronic specific heat and 5% to 10% effect on the spin-lattice relaxation rate.

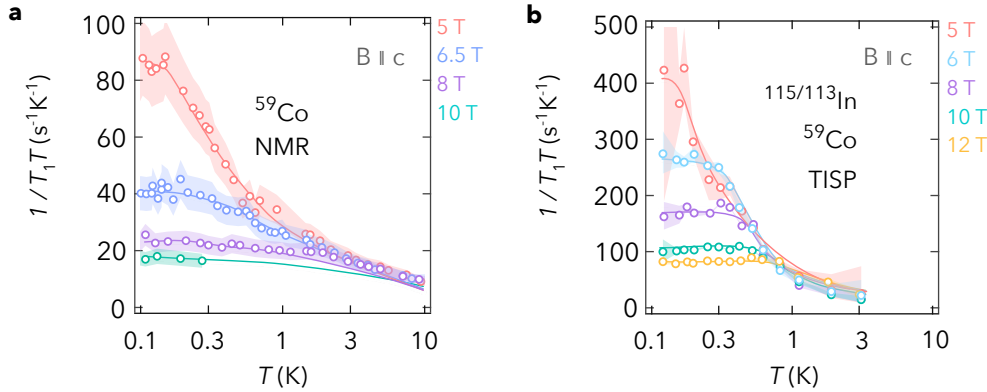


FIG. S8 **NMR measurements of  $1/T_1T$  for  $^{59}\text{Co}$  in  $\text{CeCoIn}_5$  and TISP measurements of  $1/T_1T$  for  $\text{CeCoIn}_5$ .** **a.** Nuclear spin-lattice relaxation rate of  $^{59}\text{Co}$  in  $\text{CeCoIn}_5$  from NMR measurements [14] for magnetic fields along the  $c$ -axis. **b.** TISP measurements of  $1/T_1T$  for  $\text{CeCoIn}_5$  from Figure 2 of the main text.

To investigate the effects of two nuclear components, consider a system described by equation (S1) with a fixed set of 9 parameter. We take the corresponding thermal impedance spectrum  $\zeta(\omega)_2$  and use the single-isotope model (equation (M2) in Section 4) to fit six parameters, including  $C_S$ ,  $C_N$ , and  $T_1$ .

This defines the differences  $\sigma_\eta(C_S)$ ,  $\sigma_\eta(C_N)$ ,  $\sigma_\eta(T_1)$  between the values obtained by such



fit and the corresponding model parameters in equation (S1) of the more realistic model. To calculate the  $\sigma_\eta$ 's we set

$$\begin{aligned}
 T_{11} &= T_1, \\
 T_{22} &= 5T_1 \\
 C_{2N} &= 0.13C_N \\
 C_{1N} &= 0.87C_N
 \end{aligned}
 \tag{S2}$$

where the left side corresponds to the values in equation (S1) and the right-hand side corresponds to the values in the single-isotope model (equation (M2) in Section 4). The errors  $\sigma_\eta(C_S)$ ,  $\sigma_\eta(C_N)$ ,  $\sigma_\eta(T_1)$ , evaluated at four different temperatures, are given in table I.

$T$ (K)	$\sigma_\eta(C_S)$ %	$\sigma_\eta(1/T_1T)$ %	$\sigma_\eta(C_N)$ %
0.12	0.2	7	5
0.35	0.03	6	7
1.1	0.001	5	7
3.0	0.001	4	8

TABLE I **Errors introduced by 6-parameter model.** Errors introduced by the use of a single nuclear component, evaluated at a magnetic field of 12 T along the  $ab$ -plane.

As indicated above, the values of  $\sigma_\eta(C_S)$  at temperatures above 0.3 K are much smaller than the nominal difference in the nuclear specific heat  $\sigma_\eta(C_N)$ . Importantly, the difference in  $C_S$  remains small at even lower temperatures due to the near perfect orthogonality in the parameter space (see Section 5.P for further details).

## O. Nuclear heat capacity

The nuclear specific heat is described by a high-temperature tail of a Schottky anomaly,

$$C_N = (B/T)^2 c_0, \quad (\text{S3})$$

where

$$c_0 = (1/3) N_A k_B \sum_n a_n J_n (J_n + 1) (g_n \mu_N / k_B)^2 \quad (\text{S4})$$

is the "reduced" nuclear specific heat, i.e., its value at 1 T and 1 K. The sum in equation S4 is over all nuclear species with nuclear spin in the unit cell,  $a_n$  is the number of such atoms in each unit cell.  $J_n$  and  $g_n$  are their spin and nuclear  $g$ -factors, and  $\mu_N = 32.5$  neV/T is the nuclear magneton. A small, quadrupolar contribution from In becomes important only at very small fields (below 100 mT). The value of the reduced nuclear specific heat,  $c_0 = 85 \mu\text{JK/molT}^2$ , is determined in CeCoIn<sub>5</sub> by five <sup>115</sup>In and <sup>113</sup>In nuclei (which have the same nuclear spin and very close values of the nuclear  $g$ -factor [62]) and one <sup>59</sup>Co nuclei in each unit cell. <sup>59</sup>Co accounts for about 13% of the total nuclear specific heat both because of a smaller number of cobalt atoms and because of its smaller nuclear spin [62].

At low temperatures and high magnetic fields, the measured nuclear specific heat deviates from its expected value, through an additional factor  $(1 + K)^2$  related to the knight shift  $K$ ,

$$C_N = (1 + K)^2 (B/T)^2 c_0, \quad (\text{S5})$$

describing enhanced – or screened – magnitude of local magnetic field  $(1 + K)B$ . Figure S9 shows  $(1 + K)^2$  for all fields and temperatures in Figure 2 in the main text. At low temperatures, the nuclear specific heat deviates away from its nominal value ( $K = 0$ ) by as much as a factor of two, corresponding to values of  $K$  up to  $\pm 30\%$  (see Figure S10). We currently do not exclude that some of the observed effect can arise from measurement errors and the evaluation errors due to the 6-parameter fit with a single nuclear contribution. We note, however, that such errors associated with calibration should be independent of the magnetic field orientation.

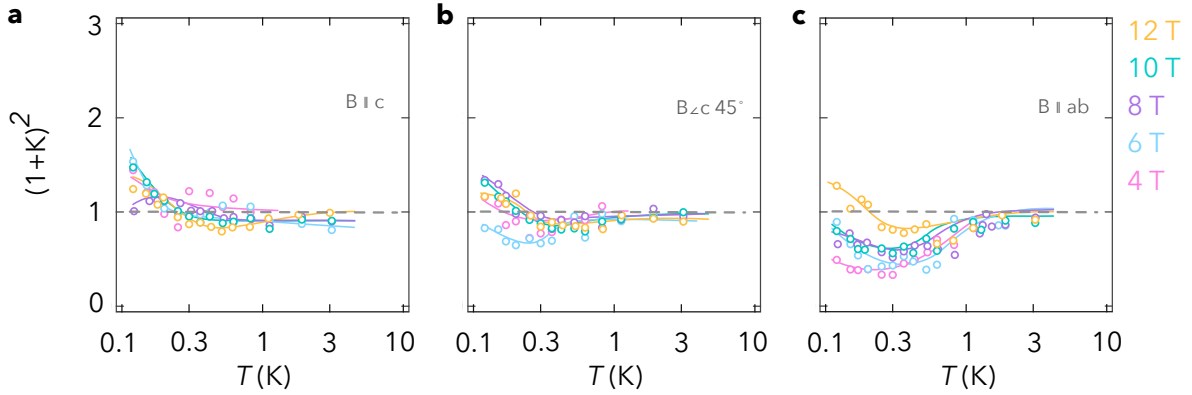


FIG. S9 **Measured nuclear specific heat normalized by its nominal value, equation (S3).**  
**a,b,c.** Nuclear specific heat (normalized by its nominal value, equation (S3)) for different magnetic fields and field orientations. The nuclear specific heat approaches its nominal value ( $K = 0$ , dashed line) at high temperatures. The deviations from the nominal value at lower temperatures indicate a difference between the applied magnetic field and the effective magnetic field at the nucleus.

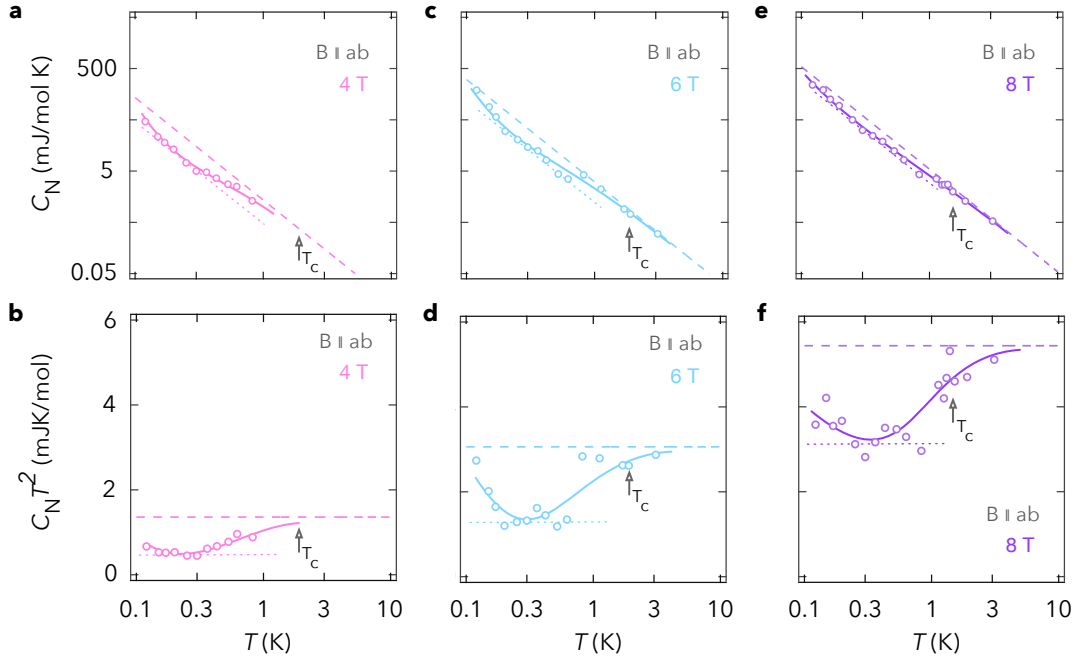


FIG. S10 **Temperature dependence of the nuclear specific heat in the superconducting and normal state of CeCoIn<sub>5</sub>.** **a,c,e.** Temperature dependence of the nuclear specific heat for fields 4, 6, and 8 T along the *ab*-plane. The dashed line indicates the nominal ( $K = 0$ ) value of nuclear specific heat. The dotted line indicates the maximum deviation of nuclear specific heat below the nominal value, more than a factor two smaller. Vertical arrows indicate the superconducting transition determined from Figure S3. All solid lines are guides for the eye. **b,d,f.** Nuclear specific heat in a,c,e plotted as  $T^2 C_N$ . The dashed line indicates the nominal behavior.

## P. Linear algebra of multiple nuclear species

The "orthogonality" of parameter space noted in Section 5.N is based on the following mathematical analysis. To cast the problem into a linear-space language we denote the observed thermal impedance spectra as  $Z(\omega)$  and the model as  $X(\omega)_{\lambda_i}$ . Both are vectors in the linear space of functions of frequency. We define a scalar product

$$\langle A(\omega)|B(\omega)\rangle \quad (\text{S6})$$

in this vector space via the frequency integrals

$$\int d\omega \beta(\omega) A(\omega)^* B(\omega). \quad (\text{S7})$$

where  $\beta(\omega)$  is a given weight function. The goodness function (Section 4) is represented by

$$g(\{\lambda_i\}) = \langle Z(\omega) - X(\omega)_{\lambda_i} | Z(\omega) - X(\omega)_{\lambda_i} \rangle. \quad (\text{S8})$$

For a perfect fit of  $Z(\omega)$  with  $X(\omega)_{\lambda_i}$ , the goodness function is at a minimum value equal to zero for small changes of all  $\lambda_i$  away from their best fit value  $\lambda_i^0$ . Now assume that the physical behavior  $Z(\omega)$  is different from the one described by the model  $X(\omega)_{\lambda_i}$ , i.e., it is described by a different model. Let the observed behavior be  $Z(\omega) + a\eta(\omega)$ , where  $a$  is a small number and  $\eta(\omega)$  is a function describing the deviation from the model  $X(\omega)_{\lambda_i}$ , i.e., we assume that  $Z(\omega)$  is fitted by the model  $X(\omega)_{\lambda_i}$  with best-fit parameters  $\lambda_i^0$ . If we do the linear regression analysis of  $Z(\omega) + a\eta(\omega)$  using the model  $X(\omega)_{\lambda_i}$ , we would find best fit parameters  $\lambda_i = \lambda_i^0 + d\lambda_i$  instead of  $\lambda_i^0$  for  $a = 0$ . What is the relation between  $d\lambda_i$ ,  $a$ , and  $\eta(\omega)$ ?

Define the new best-fit parameters from

$$\begin{aligned} & \left\langle Z(\omega) + a\eta(\omega) - X(\omega)_{\lambda_i} \middle| Z(\omega) + a\eta(\omega) - X(\omega)_{\lambda_i} \right\rangle \rightarrow \min \\ & \frac{d}{d\lambda_i} \left\langle Z(\omega) + a\eta(\omega) - X(\omega)_{\lambda_i} \middle| Z(\omega) + a\eta(\omega) - X(\omega)_{\lambda_i} \right\rangle = 0 \end{aligned} \quad (\text{S9})$$

We will only consider small values of  $a$ , for which we can truncate the expansion at the linear term,

$$\lambda_i = \lambda_i^0 + a \frac{d\lambda_i}{da}, \quad (\text{S10})$$

i.e., we assume that  $d\lambda_i$  are proportional to  $a$ . The problem is to find a set of derivatives  $d\lambda_i/da$ . Equation (S9) has a form,

$$\left\langle \frac{dX(\omega)_{\lambda_i}}{d\lambda_i} \left| Z(\omega) + a\eta(\omega) - X(\omega)_{\lambda_i} \right. \right\rangle = 0. \quad (\text{S11})$$

If  $a$  is zero, the ket in equation (S11) is identically zero for  $\lambda_i = \lambda_i^0$ . The set of six functions

$$V_i(\omega) = \left( \frac{dX(\omega)_{\lambda_i}}{d\lambda_i} \right)_{\lambda_i=\lambda_i^0} \quad (\text{S12})$$

near  $\lambda_i^0$  defines a six-dimensional ‘‘tangent’’ linear space at  $Z(\omega) = X(\omega)_{\lambda_i^0}$ . Equation (S11) can only constraint parameters  $a$  and  $d\lambda_i/da$  as long as the function  $\eta(\omega)$  can be decomposed into this tangent space. This is because small changes in  $\lambda_i$  away from  $\lambda_i^0$  produce changes in the functions  $X(\omega)_{\lambda_i}$  that lie in tangent space,  $\delta X(\omega) = d\lambda_i V_i(\omega)$ . Therefore we need to distinguish two orthogonal components of function  $\eta(\omega)$ ,

$$a\eta(\omega) = a\eta(\omega)_{\perp} + a\eta(\omega)_{\parallel}, \quad (\text{S13})$$

where  $a\eta(\omega)_{\parallel}$  is in the tangent space

$$\eta(\omega)_{\parallel} = \sum_i V_i(\omega) \eta_i \quad (\text{S14})$$

with the expansion coefficients  $\eta_i$  whereas  $\eta(\omega)_{\perp}$  is orthogonal to the tangent space,

$$\left\langle \eta(\omega)_{\perp} \left| V_i(\omega) \right. \right\rangle = 0 \quad \text{for all } i. \quad (\text{S15})$$

With this, equation (S11), is only sensitive to the tangent component  $\eta(\omega)_{\parallel}$ .

The coefficients  $\eta_i$  in equation S14 are given by

$$\eta_i = K_{ij} \left\langle \eta(\omega) \left| V_j(\omega) \right. \right\rangle, \quad K_{ij} = \left( \left\langle V_i(\omega) \left| V_j(\omega) \right. \right\rangle \right)^{-1} \quad (\text{S16})$$

where matrix  $K_{ij}$  accounts for non-orthogonality of the basis  $V_i(\omega)$  in the tangent space.

Equation (S11) now states that the tangent space component of  $\eta(\omega)_{\parallel}$  must be ‘‘balanced’’ by the small changes in the fitting parameters, which immediately results in

$$\frac{d\lambda_i}{da} = \eta_i. \quad (\text{S17})$$

where  $\eta_i$  is given by equation (S16).

A check of this result is that when the function  $\eta(\omega)$  coincides with one of the basis vectors  $V_i(\omega)$  (i.e., the modified  $Z(\omega) + a\eta(\omega)$  is still described exactly by the model  $X(\omega)_{\lambda_i}$  with simple shift in the fitting parameters), only one of  $d\lambda_i$  must be nonzero, i.e.,

$$\frac{d\lambda_i}{d\lambda_j} = \delta_{ij} \quad (\text{S18})$$

This is indeed satisfied because

$$\sum_j K_{ij} \langle V_i(\omega) | V_j(\omega) \rangle = \delta_{ij} \quad (\text{S19})$$